International Journal of Fracture **40**: 235–254, 1989.

A method for calculating stress intensities in bimaterial fracture

P.P.L. MATOS, R.M. McMEEKING, P.G. CHARALAMBIDES and M.D. DRORY
Department of Materials and Department of Mechanical Engineering, University of California, Santa Barbara, California 93106, USA

Received 15 November 1987; accepted in revised form 25 July 1988

Abstract. A numerical method is presented for obtaining the values of K_I^*, K_{II}^* and K_{III}^* in the elasticity solution at the tip of an interface crack in general states of stress. The basis of the method is an evaluation of the J-integral by the virtual crack extension method. Individual stress intensities can then be obtained from further calculations of J perturbed by small increments of the stress intensity factors. The calculations are carried out by the finite element method but minimal extra computations are required compared to those for the boundary value problem. Very accurate results are presented for a crack in the bimaterial interface and compared with other methods of evaluating the stress intensity factors. In particular, a comparison is made with stress intensity factors obtained by computing J by the virtual crack extension method but separating the modes by using the ratio of displacements on the crack surface. Both techniques work well with fine finite element meshes but the results suggest that the method that relies entirely on J-integral evaluations can be used to give reliable results for coarse meshes.

1. Introduction

In mixed mode elastic fracture mechanics it is desirable to evaluate accurately the individual mode I, II and III crack tip stress intensity factors K_I, K_{II} and K_{III} [1]. The modes are tensile opening (I), in plane shear (II) and antiplane shear (III) where the relevant plane is such that the crack front passes through it orthogonally. In addition, when a crack lies with the near tip segment in the interface between two linear elastic isotropic materials, the parameters K_I^*, K_{II}^* and K_{III}^* can be used to characterize the near tip field [2–4]. With the coordinate system aligned as in Fig. 1, the inplane stresses ahead of the crack on $x_2 = 0$ are given asymptotically by

$$\sigma_{22} + i\sigma_{12} = \frac{(K_I^* + iK_{II}^*)x_1^{i\varepsilon}}{\sqrt{2\pi x_1}}, \tag{1}$$

where

$$\varepsilon = \frac{1}{2\pi} \log \left[\left(\frac{\mu_1}{G_1} + \frac{1}{G_2} \right) \Big/ \left(\frac{\mu_2}{G_2} + \frac{1}{G_1} \right) \right] \tag{2}$$

and $i = \sqrt{-1}$. The parameters for the materials are such that G_j are the shear moduli, E_j are the Young's moduli and v_j are the Poisson's ratios. The parameters μ_j are defined so that they equal $(3 - v_j)/(1 + v_j)$ in plane stress and otherwise are $3-4v_j$. When the two materials are identical $\varepsilon = 0$ and the factors K_I^* and K_{II}^* become identical to K_I and K_{II} respectively. The antiplane stress field for the isotropic bimaterial case is unchanged from the homogeneous case, but the stress intensity factor is denoted K_{III}^* for the former for clarity.

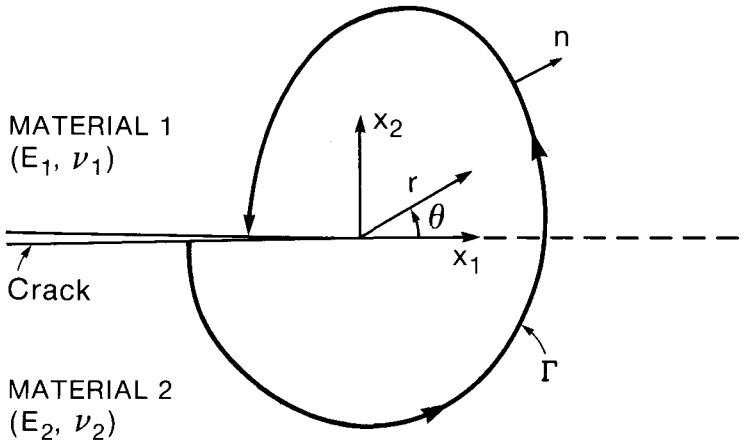

Fig. 1. Coordinates and typical contour used to evaluate the J-integral.

Henceforth, the discussion and development will be confined to the inplane stresses and displacements and the antiplane component of the near tip fields will be neglected. However, the methods addressed in this paper have obvious generalizations when there is antiplane stressing.

It is important to note that the factors K_I^* and K_{II}^* do not represent opening and shear modes [2–4]. Instead, the oscillatory nature of (1) and the associated displacements mean that the ratio of modes in the crack surface motions varies with distance from the crack tip. However, the wavelength of the oscillations increases with distance from the crack tip.

When the material interface is a plane, the J-integral [5] is path independent for the crack segment including the tip that lies in the material boundary. The relationship between $\boldsymbol{J}$ and the stress intensity factors is given by [6]

$$J = \frac{1}{H}(K_I^{*2} + K_{II}^{*2}), \tag{3a}$$

where

$$\frac{1}{H} = \frac{1}{2}\left(\frac{1}{E_1'} + \frac{1}{E_2'}\right)\Big/\cosh^2(\pi\varepsilon) \tag{3b}$$

and $E_i' = E_i$ in plane stress and $E_i' = E_i/(1 - \nu_i^2)$ in plane strain.

A review of numerical methods for obtaining the single mode stress intensity factors in the homogeneous case has been given by Gallagher [7]. The most effective of these is the virtual crack extension method of Parks [8]. However, as in all methods which evaluate $\boldsymbol{J}$ or the energy release rate, the technique must be augmented if it is to be used to establish the individual stress intensities in the mixed mode case. It is possible to define associated path independent integrals and this has been done by Ishikawa, Kitigawa and Okamura [9] for the homogeneous case. The technique was extended by Bui [10] and consists of taking the parts, symmetric and antisymmetric about the crack plane, of the planar displacement, strain and stress fields and using them separately in path integrals. One integral can be manipulated to give K_I and the other to provide K_{II}. As noted by Bui [10], the virtual crack extension

method can be used to evaluate the path integrals. However, the approach of Ishikawa et al. [9] and Bui [10] cannot be used for cracks located in bimaterial interfaces. This follows from the fact that the displacements solution in one material does not satisfy the governing equations in the other, and so the symmetric and antisymmetric parts are invalid displacements in both materials.

Yau, Wang and Corten [11] following Stern, Becker and Dunham [12] developed a technique for obtaining the separate modes by using the M_1 integral of Chen and Shield [13]. When two solutions for a given geometry are added together, a third field results for which the J-integral can be found. The value of this J differs by M_1 from the sum of the J values for the individual solutions. Thus, when one of the solutions is of a single mode of known magnitude, the value of M_1 can be used to determine one of the stress intensity factors of the other solution. Wang et al. [11] used this method for problems in homogeneous materials. They obtained the required numerical results by the finite element technique and evaluated the J and M_1 integrals by taking paths through the finite element mesh. Accurate results were obtained.

It is clear that the method of Wang et al. [11] can be used for a crack in bimaterial interface, since J and M_1 integrals still pertain. Indeed, Wang and Yau [14] applied the technique to the bimaterial case and Rice [15] has stated a line integral equivalent to M_1 specifically for the bimaterial case. Furthermore, since M_1 has J-like character, it can be evaluated by the virtual crack extension method [8]. This is desirable, since highly accurate results can be obtained at low cost in this way. Indeed Shih and Asaro [16] have recently used an equivalent method to obtain K_I^* and K_{II}^* from finite element solutions.

In this paper, a virtual crack extension based method for obtaining K_I^* and K_{II}^* from finite element solutions will be described. Results for a few problems will be presented and compared to known accurate solutions. The dependence of the accuracy on the refinement of the mesh will be investigated. Finally, results for K_I^* and K_{II}^* obtained by using crack surface displacements from finite element calculations for some problems will be compared to values resulting from the new method.

2. Formulation

The J-integral [5] is defined as

$$J = \int_\Gamma W \, dx_2 - n_i \sigma_{ij} \frac{\partial u_j}{\partial x_1} \, ds, \tag{4}$$

where Γ is any contour from the bottom crack surface around the tip to the top surface. In Fig. 1, $\mathbf{n}$ is the outward unit normal to the contour, W is the strain energy density, $\mathbf{u}$ are the displacements and ds is an infinitesimal element of contour arc length. The integral is path independent when the crack is straight, traction free and any material interface is parallel to the crack. If there are 2 displacement fields $\mathbf{u}^A$ and $\mathbf{u}^B$ representing 2 solutions to 2 different boundary value problems for the crack, the values of J associated with them are J_A and J_B. When the displacement fields are summed to give $\mathbf{u}^C$, the value of J resulting is [13].

$$J_C = J_A + J_B + M_1, \tag{5}$$

where M_1 is an integral given by

$$M_1 = \int_\Gamma \sigma_{ij}^A \varepsilon_{ij}^B \, dx_2 - \left(n_i \sigma_{ij}^B \frac{\partial u_j^A}{\partial x_1} + n_i \sigma_{ij}^A \frac{\partial u_j^B}{\partial x_1} \right) dS, \tag{6}$$

which is also path independent. From (3a), (3b) and (5) it can be deduced that

$$M_1 = \frac{2}{H} (K_{IA}^* K_{IB}^* + K_{IIA}^* K_{IIB}^*), \tag{7}$$

which was stated by Chen and Shield [13] in the homogeneous case. They also suggested that by use of a known field with $K_{IIB} = 0$, the integral could be utilized to evaluate K_{IA} for the other field, a technique taken up by Yau et al. [11]. Later, Wang and Yau [14] used known displacement fields for cracks in bimaterial interfaces along with the M_1 integral to evaluate parameters of relevance to the crack tip fields in other solutions for bimaterial cracks. However, there is an ambiguity in their results of a type addressed recently by Rice [17] relating to dimensionality and phase of the quantity $K^* = K_I^* + iK_{II}^*$.

Following Parks [8], the energy release rate definition of J can be used to develop numerical methods for its evaluation. As a result

$$J = -(\partial U/\partial a)_F \approx -\tfrac{1}{2}\{u_n\}^T (\partial [S]/\partial a) \{u_n\}, \tag{8}$$

where U is the potential energy of the body and the differentiation with respect to crack length a is carried out at fixed load. The vector $\{u_n\}$ contains as elements the nodal degrees of freedom for a finite element calculation and $[S]$ is the stiffness matrix for the mesh of elements used to solve the crack problem. In the virtual crack extension method [8] the crack problem is first solved to obtain the vector $\{u_n\}$. Then a small virtual crack extension is caused in the plane of the crack and a new value of the stiffness computed. Usually the crack is extended by rigidly moving a core of elements around the tip and distorting only one ring such as the shaded one shown in Fig. 2. That is, all elements outside the distorted ring are also held rigid. Consequently in the core of rigid elements and in the outer rigid area, $\partial [S]/\partial a = 0$. As a result, the computations of changed stiffness required are limited and the multiplication involved in (8) involves small vectors and matrices. The method has been used extensively to compute single mode stress intensity factors in the homogeneous case.

Now consider a bimaterial problem A for which it is desired to compute K_I^* and K_{II}^*. First, solve the problem by the finite element method to find $\{u_n\}$. From this, compute J by the virtual crack extension technique summarized by (8). Then add to $\{u_n\}$ the displacements $\{\Delta u_n\}_1$ for a problem in the same geometry for which $K_{II}^* = 0$ and $K_I^* = \Delta K_I^*$. This set of displacements can represent any problem desired and it should be noted that the field is actually needed only for the nodes associated with the distorted ring of elements. In view of this, the asymptotic crack tip displacements can be used everywhere as a suitable field. That is

$$\Delta \mathbf{u}_1^j = \frac{\Delta K_I^*}{2G_j} \sqrt{\frac{r}{2\pi}} \frac{e^{\pi\varepsilon}}{(1 + e^{2\pi\varepsilon})} \mathbf{f}_1 (r, \theta, \varepsilon, \mu_j), \tag{9}$$

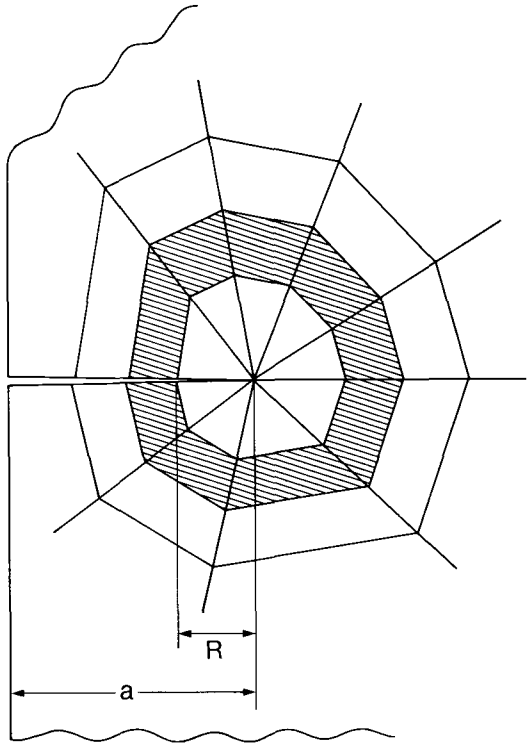

Fig. 2. A typical ring of elements to be distorted in the *J*-calculations.

where j denotes material 1 or 2 and $\mathbf{f}_j$ is described in the Appendix. The vector $\{\Delta u_n\}_1$ is obtained by evaluating (9) at the required nodes. With the value of $\partial[S]/\partial a$ already computed for the first computation of J, the calculation in (8) is repeated with the vector $\{u_n\} + \{\Delta u_n\}_1$ used instead of $\{u_n\}$ alone. The result of this calculation, $J + \Delta_1 J$, can be shown from (3), (5) and (7) to be such that

$$\Delta_1 J = \frac{1}{H}(\Delta K_1^{*2} + 2K_1^* \Delta K_1^*). \tag{10}$$

With this rearranged, it follows that

$$K_1^* = \frac{H}{2}\frac{\Delta_1 J}{\Delta K_1^*} - \frac{1}{2}\Delta K_1^* \tag{11}$$

and the 2nd term can be neglected compared to the 1st if ΔK_1^{*2} is small compared to $H\Delta_1 J$.

The procedure can then be repeated for an added vector $\{\Delta u_n\}_{II}$ such that $K_1^* = 0$ and $K_{II}^* = \Delta K_{II}^*$ if desired. These displacements are such that

$$\Delta \boldsymbol{u}_{II}^j = \frac{\Delta K_{II}^*}{2G_j}\sqrt{\frac{r}{2\pi}}\frac{e^{\pi\varepsilon}}{(1 + e^{2\pi\varepsilon})}\mathbf{f}_{II}(r, \theta, \varepsilon, \mu_j), \tag{12}$$

where $\mathbf{f}_{II}$ is described in the Appendix. Then it follows that the new value from (8) is $J + \Delta_{II}J$ and

$$K_{II}^* = \frac{H}{2}\frac{\Delta_{II}J}{\Delta K_{II}^*} - \frac{1}{2}\Delta K_{II}^*. \tag{13}$$

As an alternative, K_{II}^* can be computed directly from (3a) and (3b) given a prior calculation of J and K_I^*.

3. Implementation

The finite element calculations for each crack problem were carried out with the ABAQUS program developed by Hibbitt, Karlsson and Sorensen [18]. This code was used once to give the numerical solution ot the elastic boundary value problem for which the stress intensity factors are required. The displacement solution, nodal coordinates and element connectivity matrix produced by ABAQUS were written in a sequential output file. A separate program, called KIKII, was developed to perform the virtual crack extension calculations [8] for obtaining K_I^* and K_{II}^* as described in the previous section. KIKII selects the ring of elements to be distorted and obtains the necessary data from the ABAQUS output file. In the J-calculation subroutine of KIKII, as well as in ABAQUS, eight noded reduced integration isoparametric elements were used. Some calculations were carried out using a DEC Microvax II in double precision and others with a CONVEX CI-XP2 in standard precision. In all cases, the computer time to obtain K_I^* and K_{II}^* from the virtual crack extension calculations is negligible compared to the time needed for obtaining the finite element solution to the boundary value problem for the cracked body.

4. Numerical results

(i) *Examples.* The method was tested on two different examples. The first one consisted of an idealized problem of a circular plane strain region with a straight crack extending along the bimaterial interface from the perimeter to the center of the circle. The outer radius of the region was 10 length units. Poisson's ratio was taken to be 0.3 for the two materials and the ratio of Young's modulus in material 1 to that in material 2 was chosen to be 10. Displacement boundary conditions were imposed around the perimeter. These were exactly compatible with the asymptotic singular crack tip strains for specified values of K_I^* and K_{II}^*. They were therefore given by the sum of (9) and (12) with ΔK_I^* and ΔK_{II}^* replaced by the specified K_I^* and K_{II}^* respectively. In this way it was possible to invoke the exact boundary conditions corresponding to chosen values for K_I^*, K_{II}^* and Ψ^*, where Ψ^* is the phase angle of the stress intensity factor (arctan K_{II}^*/K_I^*).

Several calculations were done using different meshes and rings of elements to test the convergence and mesh dependence. Table 1 shows the results for K_I^*, K_{II}^* and Ψ^* and the percentage error with respect to the exact values of $K_I^* = 1.716$, $K_{II}^* = 0.208$ and $\Psi^* = 6.911$ degrees. It should be noted that the dimensions of K_I^* and K_{II}^* are stress units times length units raised to power $\frac{1}{2} - i\varepsilon$ as discussed by Rice [17]. Throughout this paper, units are omitted

Table 1. Stress intensities and percentage error for the crack in the circular plane strain region. The reported phase angle Ψ^* is in degrees

Number of elements	KIKII results			Percentage error		
	K_I^*	K_{II}^*	Ψ^*	K_I^*	K_{II}^*	Ψ^*
64	1.7162	0.2079	6.908	0.0120	0.0230	0.0003
512	1.7160	0.2080	6.9110	0.0007	0.0012	0.0
2048	1.7160	0.2080	6.9110	0.0004	0.0020	0.0

implying that an appropriate normalization has been carried out. It is observed that when refined meshes were used, the method gave highly accurate results equal to the exact ones to the fourth decimal digit. The percentage error shown in Table 1 for the very refined meshes represents presumably errors introduced at the stage of the finite element calculation. Even the relatively coarse mesh gives good results.

The second example was the case of a crack of length 2 lying along the interface of a plane stress plate subject to a normal unit tensile stress at the boundaries. One of the meshes used in this analysis to obtain the finite element elasticity solution in a plate of 20 $\times$ 20 length units is shown in Fig. 3. It has 160 elements with 64 distributed in the square focused mesh of dimension 2.0 surrounding the crack tip. Symmetry along the line $x = -1.0$ (where the crack tip is at $x = 0$) was used in order to limit the model. Table 2 lists the material properties ratios for three cases solved with this mesh. A comparison between our calculations and the analytical solution for an infinite body derived by Rice and Sih [2] is shown in Table 3. It is observed that this size of plate, 20 $\times$ 20, gives an average error of 1 percent

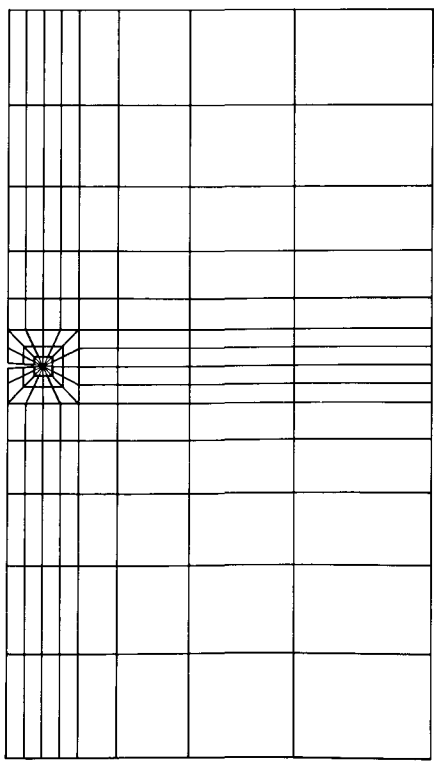

Fig. 3. Finite element mesh used in the second example.

Table 2. Material property ratios for the 20 × 20 length unit plane stress plate

Case no.	E_1/E_2	ν_1/ν_2
1	10.	1.
2	22.	0.857
3	100.	1.

Table 3. Stress intensities and percentage error for the 20 × 20 lengths units plane stress plate. The reported phase angle Ψ^* is in degrees

	Case 1			Case 2			Case 3		
	Ref. [2]	KIKII Progr.	% error	Ref. [2]	KIKII progr.	% error	Ref. [2]	KIKII progr.	% error
K_I^*	1.790	1.811	1.15	1.792	1.811	1.09	1.798	1.817	1.03
K_{II}^*	−0.217	−0.219	1.10	−0.224	−0.226	0.95	−0.262	−0.264	0.89
Ψ^*	−6.897	−6.894	0.05	−7.134	−7.124	0.13	−8.304	−8.293	0.13

Table 4. Results and percentage error for the 40 × 40 length units plate.

	K_I^*	K_{II}^*	Ψ^*
KIKII progr.	1.7953	−0.2172	−6.8995
% error	0.27	0.30	0.03

Table 5. Percentage error for different rings for the 40 × 40 length units plate

	Percentage error		
R/a	K_I^*	K_{II}^*	Ψ^*
0.04	0.26	0.36	0.09
0.09	0.27	0.32	0.05
0.16	0.27	0.32	0.04
0.34	0.28	0.32	0.04
0.44	0.28	0.29	0.02

Table 6. Percentage error for different values of ΔK_I^* and ΔK_{II}^*

$\frac{\Delta K^*}{\sqrt{J/H}}$	Circular plate		40 × 40 plate	
	Percentage error		Percentage errors	
	K_I^*	K_{II}^*	K_I^*	K_{II}^*
10^{-5}	0.730×10^{-3}	0.127×10^{-2}	0.286	0.329
10^{-4}	0.730×10^{-3}	0.127×10^{-2}	0.286	0.329
10^{-2}	0.729×10^{-3}	0.128×10^{-2}	0.286	0.329
10^{-1}	0.722×10^{-3}	0.135×10^{-2}	0.286	0.328
10^{1}	0.251×10^{-4}	0.920×10^{-2}	0.279	0.217
10^{3}	0.748×10^{-1}	0.794	0.351	10.9

for the stress intensity factors. The same crack length in a larger plate of 40 × 40 length units and using the ratio of material properties of Case 1, gives the results shown in Table 4. The mesh for this problem contained 426 elements. The average error in K_I^* and K_{II}^* is now 0.3 percent. Based on these results, one can conclude that the finite size approximation for the infinite plate makes a large contribution to the overall error shown in Table 3 and relatively little of the error is due to the technique used to evaluate the stress intensity factor. Again, good results are obtained with a coarse mesh.

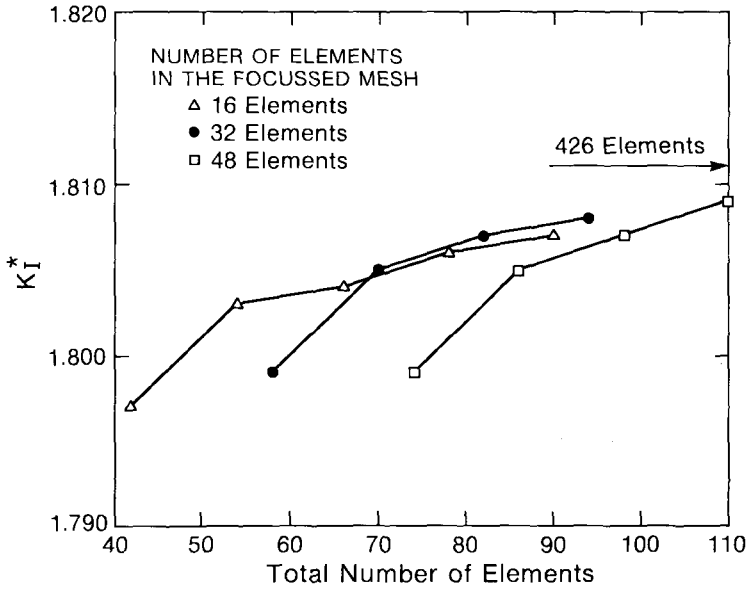

Fig. 4. Effect of the number of elements on the calculated value of K_I^*.

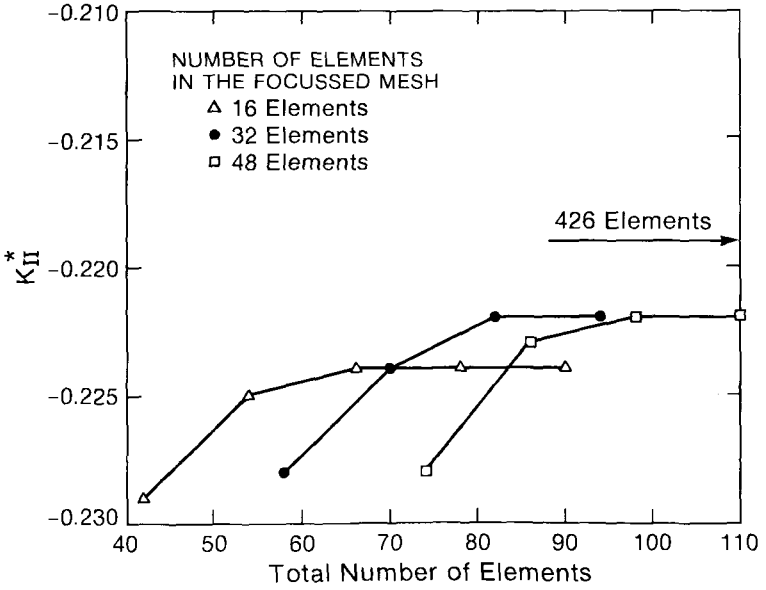

Fig. 5. Effect of the number of elements on the calculated value of K_{II}^*.

The effect of choosing different rings of elements for distortion in the virtual crack extension on the accuracy of K_I^*, K_{II}^* and Ψ^* was investigated for the 40 × 40 plate discretized in 426 elements. The percentage error compared to the infinite plate solution [2] for five different cases is shown in Table 5, in terms of R/a, the distance from the crack tip to the distorted element ring measured along the x-axis in Fig. 2 normalized by the crack length a. The accuracy of the method is independent of the choice of the ring to be distorted. Therefore, any ring can be taken, except the one containing the crack tip nodes. In this case

a singularity is introduced by the displacement increments calculated by (9) and (14) making it unsuitable for the procedure.

Convergence as a function of the stress intensity factor increments was evaluated by examining the trend in percentage error of K_I^* and K_{II}^* for both examples investigated. Table 6 shows that the method is accurate for increment magnitudes smaller than $10^{-2}\sqrt{J/H}$, for both examples presented. Even with large changes ΔK^* the results are good as long as (11) is accurately implemented.

The effect of discretization on convergence was investigated for the 20 × 20 plate using the material properties of Case 1 and mesh arrangement similar to Fig. 3. The number of elements focused at the crack tip was kept constant for a given test and the total number of elements increased by equal increments. A ring of elements within the focused mesh was distorted for the J-calculations. The results were compared with $K_I^* = 1.811$ and $K_{II}^* = -0.219$, obtained for a dense mesh of 426 elements. As Figs. 4 and 5 show, K_I^* and K_{II}^* became insensitive to the number of focussed elements as the total number of elements became large. Conversely, a lower accuracy was obtained with a small number of focussed elements. It suggests that the discretization in the near tip region has an important role in the accuracy of the method and this must be balanced with the total number of elements required for accurate results.

5. Crack surface displacement method

In this section, a different approach is used to evaluate the stress intensity factor. This method, unlike the one presented earlier, is semi-energetic; i.e. J is computed in terms of the rate of change of potential energy, whereas the phase angle Ψ^* is obtained through the crack surface displacements. The finite element node at which Ψ^* is evaluated is chosen through an internal consistency check which balances the numerical error on the displacements in the near tip region. Results obtained by this method with fine finite element meshes were in excellent agreement with those obtained via the other method. An outline of the crack surface displacement (CSD) method and its comparison with the other method are presented below.

As discussed earlier in this paper, the small strain elastic solution for the stresses in the region of an interfacial crack tip has the oscillatory character shown by (1). In accordance with (1), the crack surface displacements exhibit a similar oscillatory solution, i.e. for plane strain

$$\Delta u_2 + i\Delta u_1 = \frac{2[(1-\nu_1)/G_1 + (1-\nu_2)/G_2]}{(1+i2\varepsilon)\cosh(\pi\varepsilon)}(K_I^* + iK_{II}^*)\sqrt{\frac{r}{2\pi}}\, r^{i\varepsilon}, \tag{14}$$

where r is the distance from the crack tip. The symbol Δ on the left hand side of (14) now denotes the relative displacements of two initially neighboring points on the crack surfaces behind the tip as shown by Fig. 6. For the sake of the analysis we can rewrite the above equation as follows,

$$\|\Delta u\|\, e^{i\phi} = \alpha h^{1/2}(K_I^* + iK_{II}^*)\, h^{i\varepsilon}\left(\frac{r}{h}\right)^{1/2+i\varepsilon} e^{-i\beta}, \tag{15}$$

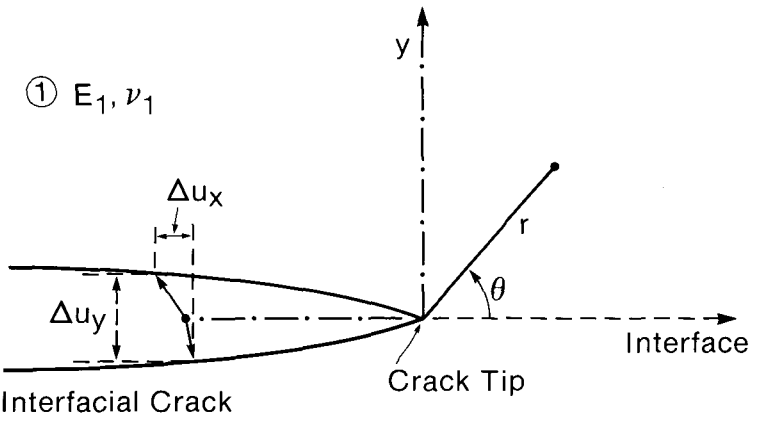

Fig. 6. The near tip crack surface displacements used in CSD method. In this figure, $\Delta u_y + i\Delta u_x = \Delta u_2 + i\Delta u_1$ used in (14) and (19).

where

$$\alpha = \frac{2[(1 - \nu_1)/G_1 + (1 - \nu_2)/G_2]}{\sqrt{2\pi(1 + 4\varepsilon^2)}\cosh(\pi\varepsilon)}. \tag{16}$$

$\|\Delta u\|$ and ϕ are the modulus and argument respectively of the complex quantity $\Delta u_2 + i\Delta u_1$, and β is the principal argument of the complex number $1 + i2\varepsilon$. As shown by (15) the product $(K_I^* + iK_{II}^*)h^{i\varepsilon}$, h being a characteristic specimen dimension, constitutes a new rotated quantity $\hat{K}_I^* + i\hat{K}_{II}^*$, with the same modulus $|K|$ as $K_I^* + iK_{II}^*$ but an augmented phase angle $\hat{\Psi}^*$ such that $\hat{\Psi}^* = \Psi^* + \varepsilon \ln h$. The new phase angle $\hat{\Psi}^*$, unlike Ψ^*, is in fact insensitive to the choice of length unit. This becomes clearer when we rewrite (15) with all complex quantities expressed in polar form, i.e.

$$\|\Delta u\| e^{i\phi} = \alpha h^{1/2} \left(\frac{r}{h}\right)^{1/2} [(K_I^*)^2 + (K_{II}^{*2})]^{1/2} e^{i} \left(\hat{\Psi}^* + \varepsilon \ln \frac{r}{h} - \beta\right), \tag{17}$$

which yields the following expressions for the scale insensitive phase angle $\hat{\Psi}^*$ and the modulus

$$\hat{\Psi}^* = \phi - \varepsilon \ln \frac{r}{h} + \beta \tag{18}$$

and

$$|K| = [(K_I^*)^2 + (K_{II}^*)^2]^{1/2} = \frac{[2\pi(1 + 4\varepsilon^2)(\Delta u_1^2 + \Delta u_2^2)]^{1/2} \cosh(\pi\varepsilon)}{2[(1 - \nu_1)/G_1 + (1 - \nu_2)/G_2]h^{1/2}(r/h)^{1/2}}. \tag{19}$$

For example, h could be the width of the specimen, rendering r/h to be a distance from the crack tip relative to the width of the specimen. The utility of this approach will become clear below.

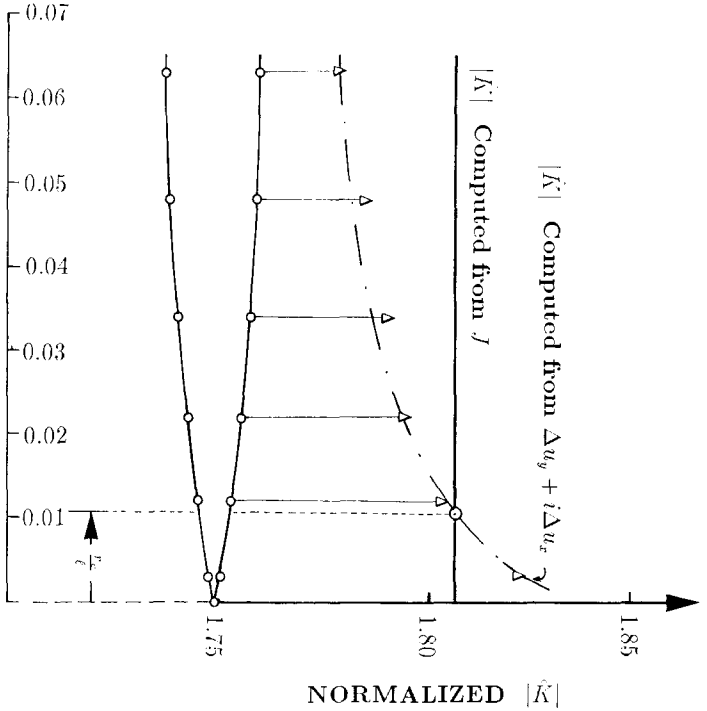

Fig. 7. The trends in the modulus $|K|$ computed from the nodal displacements (dash line) and the energy release rate (solid line). In this plot, l is the crack length, $\Delta u_x \equiv \Delta u_1$ and $\Delta u_y \equiv \Delta u_2$.

It is clear that with use of (18) and (19) finite element results for displacements $(\Delta u_1, \Delta u_2)$ along the crack surface can be used to obtain an estimate of both the phase angle $\tilde{\Psi}^*$ and the modulus $|K|$. Calculations of this type were carried out for the center cracked plate examined earlier in this work. It was found that the $|K|$ estimate, shown by the dash line in Fig. 7, varies almost linearly with r/h in the region close to the crack tip where r is now the position at which the displacements were used for (18) and (19) and h is a characteristic length taken to be one length unit. On the other hand, a very accurate estimate of $|K|$ can be obtained from the J-integral calculated by the virtual crack extension method. The relationship given by (3a) and (3b), is

$$|K| = \left[\frac{J}{\pi[(1-\nu_1)/G_1 + (1-\nu_2)/G_2]}\right]^{1/2} 2\cosh(\pi\varepsilon). \tag{20}$$

The virtual crack extension result for J and consequently for $|K|$ has been found to be independent of r/h where r is the radial position of the ring of elements distorted for this calculation. The results are shown in Fig. 7 with a solid line. As can be seen, the two estimates of $|K|$ coincide at a distance r_c, from the crack tip. Therefore, in the neighborhood r_c, nodal displacements give a good estimate of $|K|$. It is likely that the corresponding estimate for $\tilde{\Psi}^*$ given by (18) is also good at that location. Indeed, for the case of the center cracked plate, the predicted values of $|K|$ and $\tilde{\Psi}^*$ were in remarkable agreement with those found using the energy method (difference $< 0.5\%$ for $\hat{K}_1^*$) as shown in Table 7. Thus the CSD method is henceforth implemented by calculating J by the virtual crack extension method and finding

Table 7. Results for the 20 × 20 and 40 × 40 length units center cracked plate obtained via the CSD and the energy method respectively. The % error column denotes the deviation of the CSD method results from those of the energy results.

Length units		CSD method	Energy method	% error
20	K_I^*	1.810	1.811	0.05
	K_{II}^*	−0.224	−0.219	2.28
	Ψ^* (rad)	−0.123	−0.120	2.21
40	K_I^*	1.795	1.7953	0.017
	K_{II}^*	−0.222	−0.2172	2.21
	Ψ^* (rad)	−0.123	0.1204	2.20

the position on the crack for which (19) agrees with (20), where J in (20) is the virtual crack extension value. At that location, the crack surface displacements are used in (18) to compute the phase angle. The factors $\hat{K}_I^*$ and $\hat{K}_{II}^*$ are then computed by finding the real and imaginary parts of $|K|\, e^{i\Psi^*}$.

6. Comparison of the methods

The two methods were used to extract $\hat{K}_I^*$ and $\hat{K}_{II}^*$ from finite element results for the prenotched bimaterial beam in flexure shown in Fig. 8. Due to geometric and elastic symmetry with respect to its midsection, the analysis was carried out in the right half of the beam. The finite element mesh used is shown in Fig. 9 and as can be seen, in the crack tip region the mesh was focused with eight 16-element rings. The total number of elements was 1120. These elements were 8-noded isoparametric with 4-stations for the integration of the element stiffness. A series of results were obtained and tabulated (see Tables 8, 9, 10) for various crack lengths. The height h of the beam (see Fig. 8) was chosen as the characteristic specimen dimension and the values reported in the above tables correspond to the rotated stress intensity factor $\hat{K}_I^* + i\hat{K}_{II}^* = (K_I^* + iK_{II}^*)h^{i\varepsilon}$. In addition in the same tables, the stress intensity components were non-dimensionalized by $Pl/bh^{3/2}$ and the energy release rate by $P^2l^2(1 - \nu_2^2)/b^2h^3E_2$ where P is the applied load, l is the spacing between the inner and outer loading points, b is the width of the beam and E_1 the elastic modulus of the top layer (see Fig. 8).

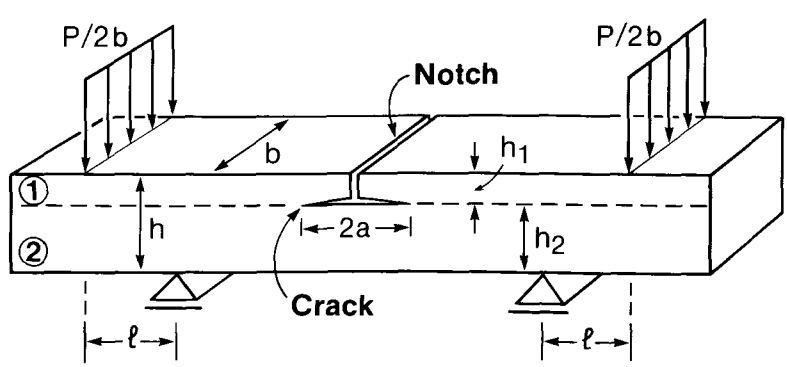

Fig. 8. The four-point bending beam with two symmetrical interfacial cracks used in the comparison of the CSD and energy methods.

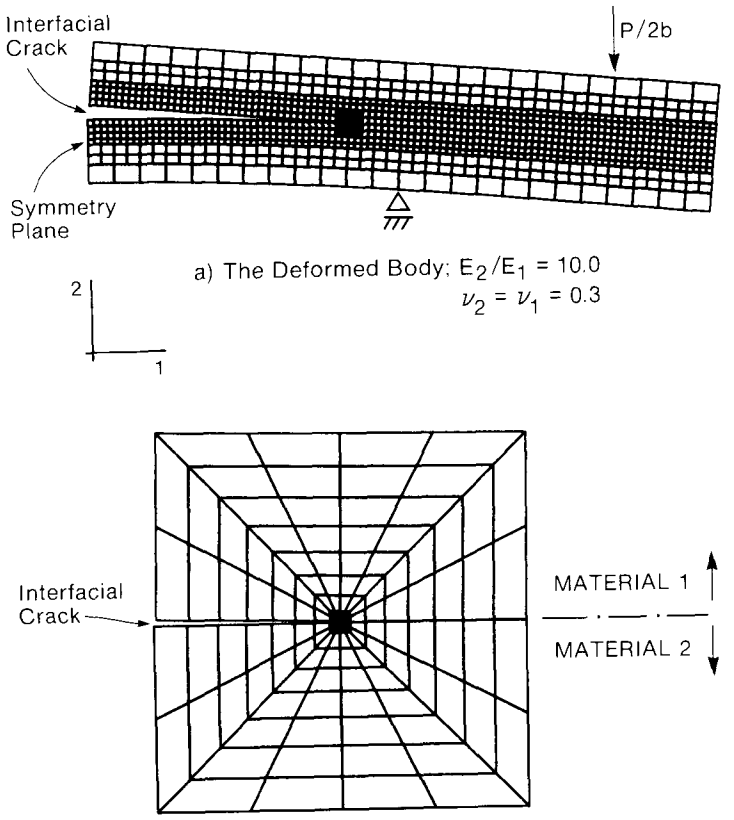

Fig. 9. The mesh used in the finite element calculations.

Table 8. The trends of the energy release rate J and normalized complex stress intensity factor K^*h^{ie} with respect to the interfacial crack length for the homogeneous case, i.e. $E_2/E_1 = 1.0$ and $\nu_2 = \nu_1 = 0.3$. Columns marked by 1 and 2 correspond to results obtained by the energy and CSD methods respectively.

E_2/E_1	a/l	J	$\hat{K}_I^*$	$\hat{K}_I^*$	$\hat{K}_{II}^*$	$\hat{K}_{II}^*$	$\hat{\Psi}^*$ (degrees)	$\hat{\Psi}^*$ (degrees)
			1	2	1	2	1	2
1.0	0.0938	10.2097	2.4501	2.4645	2.0513	2.0337	39.9363	39.5297
1.0	0.1563	10.4302	2.4478	2.4610	2.1074	2.0914	40.7262	40.3582
1.0	0.3125	10.4814	2.4484	2.4604	2.1201	2.1042	40.8904	40.5383
1.0	0.4688	10.4780	2.4487	2.4601	2.1200	2.1038	40.8849	40.5352
1.0	0.6250	10.4707	2.4498	2.4597	2.1196	2.1025	40.8674	40.5233
1.0	0.7813	10.4766	2.4535	2.4619	2.1194	2.1013	40.8206	40.4810
1.0	0.9375	10.5233	2.4626	2.4710	2.1194	2.1018	40.7160	40.3834
1.0	1.0938	10.5751	2.4736	2.4810	2.1208	2.1023	40.6090	40.2765
1.0	1.2500	10.4256	2.4477	2.4516	2.1234	2.1012	40.9415	40.5992
1.0	1.4063	9.3495	2.2530	2.2569	2.0870	2.0630	42.8090	42.4303
1.0	1.5625	6.7700	1.8376	1.8359	1.8688	1.8437	45.4817	45.1212

Table 9. The trends of the energy release rate J and normalized complex stress intensity factor K^*h^{ic} with respect to the interfacial crack length for elastic moduli ratio $E_2/E_1 = 10.0$ and Poisson's ratios $\nu_2 = \nu_1 = 0.3$. Columns marked by 1 and 2 correspond to results obtained by the energy and CSD methods respectively.

E_2/E_1	a/l	J	$\hat{K}_I^*$ 1	$\hat{K}_I^*$ 2	$\hat{K}_{II}^*$ 1	$\hat{K}_{II}^*$ 2	$\hat{\Psi}^*$ (degrees) 1	$\hat{\Psi}^*$ (degrees) 2
10.0	0.0938	6.4022	0.7830	0.7887	0.7866	0.7805	45.1305	44.6989
10.0	0.1563	6.4681	0.7701	0.7751	0.8071	0.8020	46.3443	45.9803
10.0	0.3125	6.5033	0.7685	0.7731	0.8131	0.8082	46.6153	46.2719
10.0	0.4688	6.4912	0.7678	0.7722	0.8126	0.8076	46.6239	46.2820
10.0	0.6250	6.4626	0.7662	0.7702	0.8115	0.8061	46.6427	46.3041
10.0	0.7813	6.4088	0.7628	0.7664	0.8090	0.8033	46.6860	46.3491
10.0	0.9375	6.3088	0.7554	0.7590	0.8039	0.7983	46.7805	46.4460
10.0	1.0938	6.0824	0.7388	0.7421	0.7928	0.7869	47.0178	46.6806
10.0	1.2500	5.5802	0.6997	0.7018	0.7690	0.7621	47.7024	47.3574
10.0	1.4063	4.5560	0.6114	0.6129	0.7150	0.7076	49.4657	49.1005
10.0	1.5625	3.0571	0.4800	0.4795	0.6066	0.5985	51.6449	51.3016

Table 10. The absolute percentage difference between CSD and energy method predictions. The energy results were used as datum.

a/l	$E_2/E_1 = 1.0$ $\nu_2 = \nu_1 = 0.3$			$E_2/E_1 = 10.0$ $\nu_2 = \nu_1 = 0.3$		
	$\hat{K}_I^*$ % error	$\hat{K}_{II}^*$ % error	$\hat{\Psi}^*$ % error	$\hat{K}_I^*$ % error	$\hat{K}_{II}^*$ % error	$\hat{\Psi}^*$ % error
0.0938	0.5877	0.8580	1.0181	0.7280	0.7755	0.9563
0.1563	0.5393	0.7592	0.9036	0.6493	0.6319	0.7854
0.3125	0.4901	0.7500	0.8611	0.5986	0.6026	0.7367
0.4688	0.4656	0.7642	0.8553	0.5731	j0.6153	0.7333
0.6250	0.4041	0.8068	0.8420	0.5221	0.6654	0.7259
0.7813	0.3424	0.8540	0.8319	0.4719	0.7046	0.7216
0.9375	0.3411	0.8304	0.8169	0.4766	0.6966	0.7150
1.0938	0.2992	0.8723	0.8188	0.4467	0.7442	0.7172
1.2500	0.1593	1.0455	0.8361	0.3001	0.8973	0.7232
1.4063	0.1731	1.1500	0.8846	0.2453	1.0350	0.7383
1.5625	0.0925	1.3431	0.7926	0.1042	1.3352	0.6647

A series of results were obtained for non-dimensional interfacial crack lengths in the interval $0.0938 \leqslant a/l \leqslant 1.5625$, the inner loading point being at $a/l = 1.5$. The results for the homogeneous case, i.e. $E_2/E_1 = 1.0$ are shown in Table 8 and those for $E_2/E_1 = 10.0$ in Table 9. The Poisson's ratio for all materials in both cases was chosen to be $\nu_1 = \nu_2 = 0.3$. The column indices 1 and 2 correspond to the results obtained via the energy method and CSD method respectively. In both cases, J was obtained from the stiffness derivative method [8]. For cracks in the pure bending region between the inner supports, the J values were found to be in excellent agreement with estimates obtained by Charalambides, Lund, Evans and McMeeking [19] from energy release considerations and beam bending theory.

As shown in Table 8, the $\hat{K}_I^*$ values obtained via the CSD method were consistently higher than those predicted by the energy method, and as a result, in order to maintain the same $|K|$ the corresponding $\hat{K}_{II}^*$ values predicted by the CSD method were consistently lower than those of the energy method. The absolute percentage difference denoted by % error for both $\hat{K}_I^*$ and $\hat{K}_{II}^*$ is shown in Table 10. In addition, in the same table we report on the difference in $\hat{\Psi}^*$ between the two methods. This difference was found to be of the order of 1 percent

for short cracks and 0.7 percent for cracks in the region between the inner and outer load points where the bending moment varies with crack length. In the case of a homogeneous beam, this region is dominated by the shear component stress intensity factor K_{II}. As shown in Tables 9 and 10, for both the homogeneous and the bimaterial cases, the deviation in $\hat{K}_{II}^*$ values obtained via the above methods increases as the crack approaches the transient moment region and is of the order of 1 percent for cracks between the inner and outer loading lines. On the other hand the deviation in $\hat{K}_I^*$ decreases as the crack length increases and is of the order of 0.1 percent for cracks between the inner and outer loading lines.

7. Discussion

The internal consistency check in the CSD method of using the location where the displacement based values of J agrees with the virtual crack extension J value does bring the results obtained very close to the predictions entirely based on the virtual crack extension method. Although this brings confidence to the results of both methods, this comparison is pertinent only to focused meshes with a reasonably well refined crack tip region.

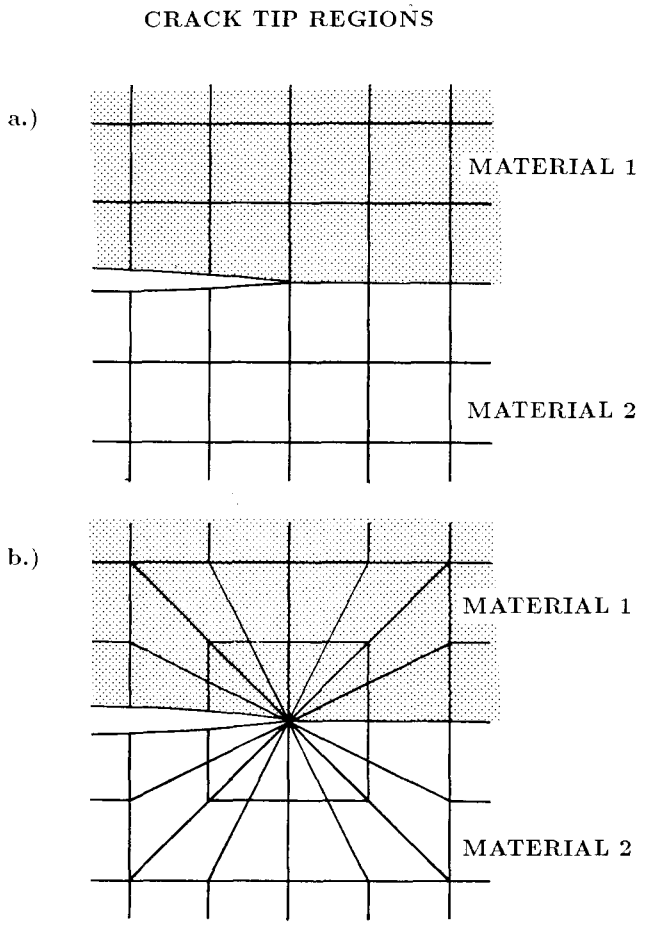

Fig. 10. The rectangular (10a) and the focused (10b) crack tip mesh used to examine the crack tip mesh type sensitivity of the CSD and energy methods.

Table 11. Selective results for two different crack lengths obtained by the CSD method. Columns 1 and 2 correspond to the crack tip mesh type shown in Fig. (10b) and Fig. (10a) respectively.

E_2/E_1	a/l	J	J	$\hat{K}_I^*$	$\hat{K}_I^*$	$\hat{K}_{II}^*$	$\hat{K}_{II}^*$	$\hat{\Psi}^*$ (degrees)	$\hat{\Psi}^*$ (degrees)
		1	2	1	2	1	2	1	2
1.0	0.9375	10.5233	10.5692	2.4710	2.5080	2.1018	2.0710	40.3834	39.5513
1.0	1.4063	9.3495	9.4494	2.2569	2.2990	2.0630	2.0330	42.4303	41.4879
10.0	0.9375	6.3088	6.2583	0.7590	0.8370	0.7983	0.6840	46.4460	39.2647
10.0	1.4063	4.5560	4.4524	0.6129	0.6690	0.7076	0.6130	49.1005	42.7254

Table 12. The absolute percentage difference marked as % error between the CSD results for the mesh type 10a and 10b, the second being the datum.

E_2/E_1	a/l	J % error	$\hat{K}_I^*$ % error	$\hat{K}_{II}^*$ % error	$\hat{\Psi}^*$ % error
1.0	0.9375	0.4362	1.4974	1.4654	2.0605
1.0	1.4063	1.0685	1.8654	1.4542	2.2210
10.0	0.9375	0.8005	10.2767	14.3179	15.4616
10.0	1.4063	2.2743	9.1532	13.3691	12.9836

For example, Charalambides et al. [20] reported K^* values for the same specimen geometry using a rectangular mesh in conjunction with the CSD method. In that analysis the elements used were also 8-noded isoparametric and the crack tip region was discretized as shown schematically in Fig. 10a, whereas the results reported earlier in this paper were obtained for the focused crack tip mesh shown schematically in Fig. 10b. Overall, the mesh containing the near tip region shown in Fig. 10a had a total of 1232 elements versus a total of 1120 in the focused mesh. Selective results for two crack lengths and two moduli ratios, i.e. $E_2/E_1 = 1.0, 10.0$ are presented in Tables 11 and 12. The columns marked by the index 1 correspond to the focused mesh results and those marked by 2 represent the rectangular mesh results. Here, as before, we use the same non-dimensional quantities. In Table 12, the % error mark denotes the absolute percentage difference of the rectangular mesh results relative to those of the focused mesh. As we can see in the table, the rectangular mesh predictions are most in error compared to the results of the energy method although bounded by a maximum deviation of 15 percent. It is also of some interest to notice that the J estimates from the rectangular mesh are slightly different from those obtained using a focused mesh. This may be an indication of the expected mesh sensitivity of the energy method when used in conjunction with a rectangular mesh. In that respect these results are very encouraging as far as the energy method is concerned since the J estimates appear to be rather mesh insensitive.

A previous analysis (see Figs. 4 and 5) showed that the energy method, unlike the CSD method, depends very little on the number of finite elements or the element ring used, especially when the total number of elements is greater than 50. These results, in light of the rectangular mesh results, suggest that the energy method is indeed very powerful in estimating stress intensities at interfacial crack tips even when used in conjunction with coarse meshes. On the other hand, the CSD method when used with focused meshes, also provides a reliable technique for extracting the stress intensity factors. However, in the latter case, one should be aware of the dependency of the results on the number of elements in the finite element mesh and that it is less accurate for meshes with less than 300 8-noded isoparametric elements.

8. Conclusions

Two methods for evaluating the stress intensity factors for crack tips were presented. An advantage of the methods is that they are general and can be used for cracks on bimaterial interfaces. A finite element solution for the crack problem is required in both methods. Thereafter, the computations for the evaluation of the stress intensity factors consist only of a very small fraction of those required to obtain the finite element solution for the crack problem. As a result predictions of high accuracy can be obtained at minimum cost. The crack surface displacement method was found to be more sensitive to mesh refinement and mesh-type in the tip region than the energy method. This is an expected result since the J-calculations are, in general, mesh insensitive. This makes the energy method a more attractive one especially when the crack problem finite element solution is obtained using a coarse mesh.

Acknowledgement

The authors wish to thank Hibbitt, Karlsson and Sorensen Inc. of Providence, R. I. for the provision of the ABAQUS code used for all the finite element calculations. Financial support was provided by the Defense Advanced Research Projects Agency through the University Research Initiative of UCSB under Contract N-00014-86-K-0753.

Appendix

The components of the functions $f_{\mathrm{I}}(r, \theta, \varepsilon, \mu_j)$ and $f_{\mathrm{II}}(r, \theta, \varepsilon, \mu_j)$ that introduce the oscillatory characteristic of the near crack tip displacement field are obtained as follows:

$$f_{1\mathrm{I}} = D_j + 2\delta_j \sin\theta \sin\Psi \tag{A1}$$

$$f_{2\mathrm{I}} = -C_j - 2\delta_j \sin\theta \cos\Psi \tag{A2}$$

and

$$f_{1\mathrm{II}} = -C_j + 2\delta_j \sin\theta \cos\Psi \tag{A3}$$

$$f_{2\mathrm{II}} = -D_j + 2\delta_j \sin\theta \sin\Psi. \tag{A4}$$

D_j, C_j, d_j and Ψ are defined as

$$\delta_1 = \mathrm{e}^{-(\pi-\theta)\varepsilon} \quad \delta_2 = \mathrm{e}^{(\pi+\theta)\varepsilon}$$

$$\Psi = \varepsilon \log r + \frac{\theta}{2}$$

$$D_j = \beta\gamma_j \cos\frac{\theta}{2} + \beta'\gamma_j' \sin\frac{\theta}{2}$$

$$C_j = \beta'\gamma_j \cos\frac{\theta}{2} - \beta\gamma_j' \sin\frac{\theta}{2}$$

$$\beta = \frac{0.5 \cos(\varepsilon \log r) + \varepsilon \sin(\varepsilon \log r)}{0.25 + \varepsilon^2}$$

$$\beta' = \frac{0.5 \sin(\varepsilon \log r) - \varepsilon \cos(\varepsilon \log r)}{0.25 + \varepsilon^2}$$

$$\gamma_j = \mu_j\delta_j - \frac{1}{\delta_j} \quad \gamma_j' = \mu_j\delta_j + \frac{1}{\delta_j},$$

where (r, θ) are the polar coordinates as shown in Fig. 1, ε is the bimaterial constant as defined before and j is the material index.

References

1. M.F. Kanninen and C.H. Popelar, *Advanced Fracture Mechanics*, Oxford University Press, New York (1985).
2. J.R. Rice and G.C. Sih, *Journal of Applied Mechanics* 32 (1965) 418–423.
3. F. Erdogan, *Journal of Applied Mechanics* 30 (1963) 232–236, and *ibid* 32 (1965) 403–410.
4. A.H. England, *Journal of Applied Mechanics* 32 (1965) 400–402.
5. J.R. Rice, *Journal of Applied Mechanics* 35 (1968) 379–386.
6. J.R. Willis, *Journal of the Mechanics and Physics of Solids* 19 (1971) 353–368.
7. R.H. Gallagher, in *Numerical Methods in Fracture Mechanics*, Proceedings of the First International Conference, Swansea (1978) 1–25.
8. D.M. Parks, *International Journal of Fracture* 10 (1974) 487–502.
9. H. Ishikawa, H. Kitigawa and H. Okamura, in *Mechanical Behavior of Materials*, Proceedings of the Third International Conference held in Cambridge, England, K.J. Miller and R.F. Smith (eds.), Vol. 3, Pergamon (1979) 447–455.
10. H.D. Bui, *Journal of Mechanics and Physics of Solids* 31 (1983) 439–448.
11. J.F. Yau, S.S. Wang and H.T. Corten, *Journal of Applied Mechanics* 47 (1980) 335–341.
12. M. Stern, E.B. Becker, and R.S. Dunham, *International Journal of Fracture* 12 (1976) 359–368.
13. F.H.K. Chen and R.T. Shield, *Zeitschrift fuer angewandte Mathematik und Physik* 28 (1977) 1–22.
14. S.S. Wang and J.F. Yau, *AIAA Journal* 19 (1981) 1350–1356.
15. J.R. Rice, private communication, 1986.
16. C.F. Shih and R.J. Asaro, "Elastic-Plastic Analysis of Cracks on Bimaterial Interfaces Part I: Small Scale Yielding", Report (1987).
17. J.R. Rice, *Journal of Applied Mechanics* 55 (1988) 98–103.
18. H.D. Hibbitt, B. Karlsson and E.P. Sorensen, *User's Manual*, Hibbitt, Karlsson and Sorensen Inc., Providence RI (1984).
19. P.G. Charalambides, J. Lund, A.G. Evans and R.M. McMeeking, *Journal of Applied Mechanics* 56 (1989) 77–82.
20. P.G. Charalambides, J. Lund, A.G. Evans and R.M. McMeeking, "A Test Specimen for Determining the Fracture Resistance of Bimaterial Interfaces." *The Processing and Mechanical Properties of High Temperature/High Performance Composites.* Annual Report, Department of Materials, University of California at Santa Barbara (1987).

Résumé. On présente une méthode numérique en vue d'obtenir les valeurs de K_I^*, K_{II}^* et K_{III}^* relatives à la solution élastique d'application à l'extrémité d'une fissure d'interface sujette à un état de contraintes général. La méthode repose sur l'évaluation de l'intégrale J par la technique d'extension virtuelle de la fissure. On peut ensuite obtenir les intensités de contraintes individuelles à partir de calculs de J subséquents, correspondant à des perturbations introduites par de petits accroissements des facteurs d'intensité de contraintes.

Les calculs sont accomplis par la méthode des éléments finis, mais, par rapport aux calculs à mettre en oeuvre dans le problème des valeurs aux limites, il ne faut procéder qu'à quelques calculs supplémentaires.

On présente des résultats très précis pour le cas d'une fissure dans un interface entre deux matériaux, et on les compare avec ceux provenant d'autres méthodes d'évaluation des facteurs d'intensité de contraintes.

En particulier, on fait une comparaison pour des facteurs d'intensité de contraintes obtenus en calculant J par la méthode d'extension virtuelle d'une fissure, mais en séparant les modes selon le rapport des déplacements de la surface de la fissure.

Les deux techniques fonctionnent de manière satisfaisante avec des maillages fins d'éléments finis; cependant, les résultats suggèrent que la méthode qui repose entièrement sur les évaluations de l'intégrale J peut être utilisée afin d'obtenir des résultats fiables dans les réseaux à mailles grossières.